Sustainable Energy & Fuels

Solution plasma synthesis of perovskite hydroxide $CoSn(OH)_6$ nanocube electrocatalysts toward oxygen evolution reaction

Journal:	*Sustainable Energy & Fuels*
Manuscript ID	SE-ART-02-2023-000221.R1
Article Type:	Paper
Date Submitted by the Author:	06-Apr-2023
Complete List of Authors:	Narahara, Masaki; Shibaura Institute of Technology, Materials Science and Engineering, Graduate School of Engineering and Science, Shibaura Institute of Technology Lee, So Yoon; Shibaura Institute of Technology - Toyosu Campus, Department of Materials Science and Engineering Sasaki, Kodai ; Shibaura Institute of Technology - Toyosu Campus, Materials Science and Engineering, Graduate School of Engineering and Science Fukushima, Kaito ; Shibaura Institute of Technology, Materials Science and Engineering, Graduate School of Engineering and Science Tanaka, Kenichi ; Shibaura Institute of Technology, Materials Science and Engineering, Graduate School of Engineering and Science Chae, Sangwoo ; Shibaura Institute of Technology, SIT Research Laboratories Hu, Xiulan ; Nanjing Tech University College of Materials Science and Engineering Panomsuwan, Gasidit; Kasetsart University, Department of Maerials Engineering Ishizaki, Takahiro; Shibaura Institute of Technology, Department of Material Science and Engineering, Faculty of Engineering,

Solution plasma synthesis of perovskite hydroxide $CoSn(OH)_6$ nanocube electrocatalysts toward oxygen evolution reaction

Masaki Narahara[1], So Yoon Lee[2], Kodai Sasaki[1], Kaito Fukushima[1], Kenichi Tanaka[1], Sangwoo Chae[3], Xiulan Hu[4], Gasidit Panomsuwan[5], Takahiro Ishizaki[2,]*

[1]Materials Science and Engineering, Graduate School of Engineering and Science, Shibaura Institute of Technology, Tokyo 135-8548, Japan

[2]Department of Materials Science and Engineering, College of Engineering, Shibaura Institute of Technology, Tokyo 135-8548, Japan

[3]SIT Research Laboratories, Shibaura Institute of Technology, Tokyo 135-8548, Japan

[4]College of Materials Science and Engineering, Nanjing Tech University, Nanjing 211816, China

[5]Department of Materials Engineering, Faculty of Engineering, Kasetsart University, Bangkok 10900, Thailand

ABSTRACT: To realize high-performance lithium–air batteries, it is necessary to develop a catalyst material that promotes the redox reaction of oxygen. Perovskite-type oxides and hydroxides are known as catalyst materials for accelerating the oxygen evolution reaction (OER). $CoSn(OH)_6$ (CSO) is a perovskite-type hydroxide that is a promising catalyst for the OER. In this study, the synthesis and characterization of CSO using a solution plasma process was reported. By using this process, the CSO could be synthesized in 20 min. X-ray diffractometry (XRD) results revealed that highly crystalline CSO can be synthesized by adjusting the pH of the precursor solution of more than 10 to 12. The synthesized CSO had a cubic shape and its size was approximately 100 to 300 nm. X-ray photoelectron spectroscopy (XPS) results showed that the valences of Co and Sn in CSO were divalent and tetravalent, respectively. The catalytic properties of the synthesized CSO for the OER were evaluated using an electrochemical method. The overpotential at 10 mA/cm^2 and Tafel gradient of the synthesized samples at pH12 (CSO_pH12sp) were estimated to be 350 mV and 69.58 mV/decade, respectively. The CSO_pH12sp sample

showed most superior catalytic property among all samples synthesized and the catalytic property was slightly superior to commercial RuO_2. The potential reached 10 mA/cm^2 of the synthesized samples at CSO_pH12sp had the lowest potential, which was 104 mV vs. RHE more positive than that of commercially available RuO_2. From the results of optical emission spectroscopy, the active species formed in the plasma were clarified and the mechanism of CSO synthesis was discussed based on the active species.

1. Introduction

Lithium–air batteries have a high theoretical energy density; therefore, they are expected to be next-generation batteries that can replace lithium-ion batteries.[1] However, to put a lithium–air battery to practical use, it is necessary to solve problems such as improvement of energy efficiency and cycle characteristics, and reduction of overpotential required for the charge/discharge reaction.[2] To solve these problems, it is necessary to develop a catalytic

material to efficiently carry out the redox reaction of oxygen, which is important in the charge/discharge reaction of the lithium–air batteries. In lithium–air batteries, the redox reaction of oxygen is utilized to form and decompose Li_2O_2 at the positive electrode.[3,4] Therefore, it is important to promote the redox reaction of oxygen, and the development of a catalytic material for this purpose is indispensable. Carbon materials and metal oxides have attracted attention as catalysts for oxygen reduction and oxidation reactions.[5-10] Carbon materials are used as catalytic materials to promote the oxygen reduction reaction (ORR) associated with the discharge reaction. Carbon materials that are compound-doped with N, B, P, and these dissimilar elements have been developed and have achieved high performance in the ORR.[11-18] In addition, it is possible to improve the ORR characteristics by including a metal-N-C bond in the carbon material.[19-24]

Noble metal oxides such as RuO_2 and IrO_2 have been used as catalyst materials for the oxygen evolution reaction (OER) of metal–air cells, but these compounds have problems in terms of resource quantity and raw material cost, so they are scarcer and more expensive. The development of catalyst materials consisting of abundant elements is underway.[25] Transition metal oxides have attracted much attention as catalyst materials for the OER. It is well known

that transition metal oxides, such as Co_3O_4, are catalysts for reactions such as the ORR and OER. This phenomenon arises from the energy level; in detail, the energy levels of the $3d$ orbitals of transition metals and the $2p$ orbitals of oxide ions are close to each other, and the charge is easily transferred.[26] Perovskite-, spinel-, and pyrochlore-type oxides are transfer metal oxides, and these transition metal oxides have been reported to be highly active for the OER.[26] In particular, perovskite-type oxides are being actively studied as promising candidate substances, and their catalytic activity for oxygen evolution has been discussed based on a strong correlation between the crystal structure,[27-29] electronic states,[30,31] and the presence or absence of oxygen deficiency.[32] In addition, because of their high flexibility in terms of chemical composition and local structure, they exhibit a wide variety of electronic properties and are promising materials for obtaining excellent OER catalysts. $CoSn(OH)_6$ (CSO) is a perovskite-type hydroxide that exhibits superior OER activity.[33] In particular, the formation of a nanocrystalline structure and imparting a porous structure to increase the surface area can improve the OER activity. Song et al. produced $CoSn(OH)_6$ by the co-precipitation method and reported that $CoSn(OH)_6$ showed poor OER activity.[33] However, the electrocatalytic activity of the $CoSn(OH)_6$ for OER was greatly improved by an electrochemical preconditioning through 80 cyclic voltammetric scans

(CVs) and galvanostatic activation.[33] Lin et al. also reported that $CoSn(OH)_6$ was produced by the co-precipitation method and showed an improvement in the catalytic performance for CO_2.[34] However, these methods require more than half a day or multistep treatment to synthesize $CoSn(OH)_6$. In addition, considering the application of $CoSn(OH)_6$ to Li-air battery, to improve the performance of the Li-air battery, the development of composite materials composed of $CoSn(OH)_6$ and electrocatalytic material for ORR would be required. From this point of view, it is necessary to develop a method for synthesizing $CoSn(OH)_6$ in a shorter time and lower steps.

Solution plasma (SP) is a nonthermal equilibrium plasma generated by a glow discharge in a solution. Because the SP is a nonthermal equilibrium plasma, the ion temperature is lower than the electron temperature, and the increase in the solution temperature based on heat diffusion from reaction field. For this reason, it is a unique method for material synthesis in a low-temperature reaction field using a solution, which is difficult with a gas-phase plasma or a high-temperature plasma in a liquid. Furthermore, this process can reduce the processing time and step required for material synthesis. Therefore, it is used for the synthesis of metal nanoparticles and composite materials of metal nanoparticles,[35] decomposition of sugar chain polymers,[36] synthesis of nanocarbon materials and surface treatment,[37-43] and synthesis of heteroatom-doped carbon

materials.[44-46] In addition, SP can synthesize composite materials at a singlestep. Panomsuwan et al. reported a single step SP synthesis of carbon-based composite material.[47,48] Thus, SP is considered to be suitable for the synthesis of composite materials.

In this paper, we report on the SP synthesis and evaluation of CSO, and electrocatalytic performance of the obtained materials for the OER.

2. Experimental

2.1 Synthesis of CSO

Perovskite hydroxide $CoSn(OH)_6$ (CSO) nanocubes were synthesized by co-precipitation and solution plasma (SP) to compare the chatracterization and the electrocatalytic performance of the samples synthesized by each synthesis method. In the SP synthesis, cobalt chloride ($CoCl_2$: Kanto Chemical Co., Inc., Japan) and tin chloride (IV) pentahydrate ($SnCl_4 \cdot 5H_2O$: Kanto Chemical Co., Inc., Japan) were used as the raw materials for $CoSn(OH)_6$ (CSO) synthesis. The Co and Sn sources were each dissolved in 100 mL of ultrapure water to obtain a 0.01 M aqueous solution. The pH was adjusted to 8, 9, 10, and 12 with 1 M aqueous sodium hydroxide solution (NaOH: Kanto Chemical Co., Inc., Japan). Two tungsten electrodes (ϕ1 mm)

were fixed to the SP rection cell at a distance of 0.5 mm such that they faced each other, and the sides of each electrode were covered with an insulator. Using a bipolar pulse power supply (MPP-HV04, Kurita Seisakusho), plasma was generated for 20 min under the conditions of an applied voltage of 1.2 kV, a pulse width of 0.8 μs, and a frequency of 50 kHz. After the synthesis by SP, the cells were filtered using a hydrophilic PTFE membrane filter (KENIS, 0.1 μm pore diameter) and thoroughly washed with ultrapure water and ethanol. After washing, the recovered sample was heated in an electric furnace at 60 ˚C for 12 h and dried. The obtained sample was crushed in an agate mortar to obtain the sample for analysis. In co-precipitation synthesis, 5 ml of an aqueous solution containing $SnCl_4 \cdot 5H_2O$ (0.2 M) was added to 35 ml of an aqueous solution containing $CoCl_2$ (1 mM) and the mixed solution was stirred for 30 minutes, and then the pH was adjusted to 8, 9, 10, and 12 by drop-wise addition of 10 mL of NaOH solution (2 M) under the stirring condition. After that, the mixed solution was further stirred for 1 hour at room temperature resulting in the formation of precipitation. The mixed solution containing the precipitation was filtered using a hydrophilic PTFE membrane filter (KENIS, 0.1 μm pore diameter) and thoroughly washed with ultrapure water and ethanol three times. After washing, the recovered sample was heated in an electric furnace at 80 ˚C for 12 h and dried. Hereinafter,

the sample name includes the pH value of the precursor solution and synthesis method (solution plasma as “sp” and co-precipitation as “p”) as follows: CSO_pH8sp, CSO_pH9sp, CSO_pH10sp, CSO_pH12sp, CSO_pH8p, CSO_pH9p, CSO_pH10p, and CSO_pH12p.

2.2 Characterization of synthesized samples

The crystal structures of the synthesized samples were identified using X-ray diffractometry (XRD, Rigaku, Smart Lab, Tokyo, Japan). The XRD measurements were performed at a voltage of 40 kV and a current of 30 mA using Cu Kα X-rays within the range of $2\theta = 5^{\circ}$–90°. The scanning speed was 5˚/min. A qualitative analysis of the bonding states and substances was performed using X-ray photoelectron spectrometry (XPS, JEOL Ltd., Tokyo, Japan). XPS measurements were performed using monochromatic Mg Kα radiation (1253.6 eV) as an excitation source under ultra-high vacuum conditions at a voltage of 10 kV and a current of 25 mA. The obtained spectra were corrected for charge-up using the 284.6 eV peak of the C 1s spectrum. The shape of the samples was observed using scanning electron microscopy (FE-SEM, JEOL, JSM-7610F, JEOL Ltd., Tokyo, Japan) and transmission electron microscopy (TEM,

JEM-2100, JEOL, Tokyo, Japan). The radical species generated by plasma in liquid were measured by optical emission spectroscopy (OES, AVANTES, AvaSpec-3648).

2.3 OER catalyst performance evaluation

Linear sweep voltammetry (LSV) measurements were performed using an electrochemical measuring device (BAS Co., Ltd., ALS704ES) to evaluate the catalytic performance of the synthesized samples for the OER. The catalyst ink was prepared by dispersing 5 mg of synthesized sample in a mixture of 500 μL ethanol and 50 μL of Nafion® DE521 aqueous solution, followed by sonication for 10 min to form a suspension. The resulting sample suspension was carefully dropped onto a glassy carbon disk electrode (disk diameter: 4 mm, A_{disk} = 0.126 cm^2) surrounded by a Pt ring (inner/outer-ring diameter: 5.0/7.0 mm, Aring = 0.188 cm^2) with a Teflon separator (rotating ring disk electrode, RRDE, ALS Co.). After drying, the resulting electrode was used as the working electrode. Ag/AgCl and a platinum coil were used as the reference and counter electrodes, respectively. As a control, the electrocatalytic activity for OER of commercial RuO_2 powder were also measured. The working electrode with commercial

RuO_2 powder (Fujifilm Wako Pure Chemical Co.,) was prepared using the same method as mentioned above. A 0.1 $mol \cdot L^{-1}$ potassium hydroxide solution was used as the electrolytic solution. For all measurements, the electrolytic solution was bubbled with nitrogen gas for 20 min to remove dissolved oxygen and then bubbled with oxygen gas for 20 min. The O_2 gas was passed on the solution level in the electrochemical cell during the measurements. In the LSV measurement, the scan rate was set to 10 $mV \cdot s^{-1}$. All the experiments were performed at room temperature.

3. Results and discussion

Figure 1 shows the XRD patterns of the samples synthesized by SP under each condition. As shown in Fig. 1, the CSO_pH8sp samples showed broad peaks derived from SnO_2 (JCPDS card no. 77-0452) at near $2\theta = 26^\circ$, 34°, 52°, and 64°, and no peaks derived from Co can be observed. This indicates that SnO_2 with low crystallinity was formed in the CSO_pH8sp samples. In the case of the CSO_pH9sp sample, in addition to a few broad peaks derived from SnO_2, two weak peaks assigned to CoOOH (JCPDS card no. 07-0169) were also detected at approximately $2\theta =$

20 and 82˚. This indicates that CSO_pH9 formed SnO_2 and CoOOH with low crystallinity. Some peaks at around 2θ = 23, 33, 46, 52, and 74° can be observed in the XRD profiles of CSO_pH10sp and CSO_pH12sp. These peaks are assigned to the perovskite-type hydroxide $CoSn(OH)_6$ (JCPDS card no. 13-0356), indicating that crystalline $CoSn(OH)_6$ was formed in the samples of CSO_pH10sp and CSO_pH12sp. In particular, in the CSO_pH12sp sample, the half-width of the peak is narrow, and its intensity is high, and thus it is considered that CSO with high crystallinity was formed. In addition, a broad and weak peak attributable to Co_3O_4 (JCPDS card no. 78-1969) can be also observed at approximately 2θ = 44°, indicating that Co_3O_4 could be locally formed in the CSO_pH12sp sample. Figure S1 shows the XRD patterns of the samples synthesized by the co-precipitation method from aquesou solutions at different pH. Similar to the SP method, it was confirmed that crystalline $CoSn(OH)_6$ was formed in the samples synthesized at CSO_pH10p and CSO_pH12p, and SnO_2 with low crystallinity was formed at CSO_pH8p and CSO_pH9p. However, the main crystal phase of the CSO_pH10p was SnO_2 with low crystallinity and different from that of the CSO_pH10sp. This difference could occur due to the the difference in the synthesis method.

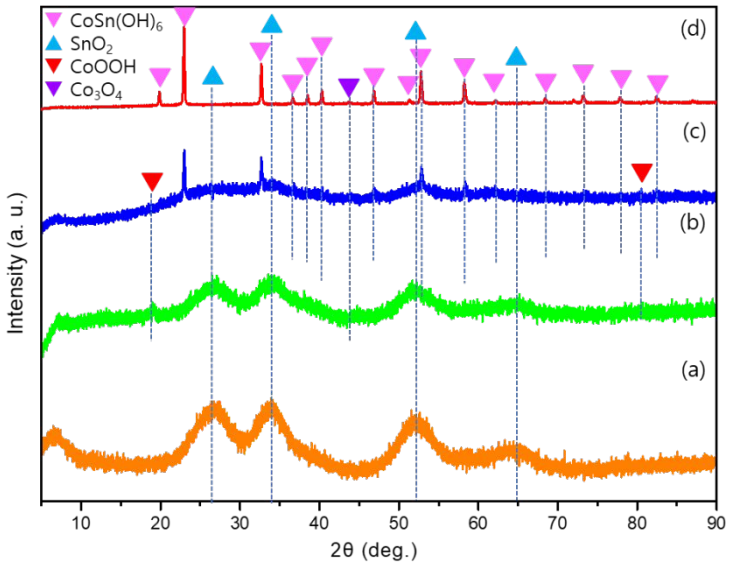

Figure 1. XRD patterns of samples synthesized by SP at different pH; (a) CSO_ pH8sp, (b) CSO_pH9sp, (c) CSO_ pH 10sp, and (d) CSO_ pH 12sp.

Figure 2 and S2 show FE-SEM images of the samples synthesized by SP and co-precipitation method under each condition. From Fig. 2 and S2, it was confirmed that the samples of CSO_pH8sp, CSO_pH8p, CSO_pH9sp, and CSO_pH9p had amorphous or low-crystallinity amorphous structures. The sizes of these samples were in the ranges of 30 to 500 nm. Amorphous and crystalline cubic-like structures were mixed in the samples of CSO_pH10sp, CSO_pH10p, CSO_pH12sp, and CSO_pH12p. In particular, the sample of CSO_pH12sp and CSO_pH12p had many cubic-like structures. The particle sizes of CSO_pH12sp were ranged from 50 to 100 nm, while the particle sizes of CSO_pH12p were in

the rages of 100 to 200 nm (Figure S2). This result means that the sizes of the products synthesized by SP were smaller than those by co-precipitaiton method. The difference in the size of the products can be due to the difference in the input energy to reaction field. In the reaction field by SP, the input energy is high, so the nucleation would occurred more preferential than the crystal growth, thus resulting in the formation of the products with smaller size. Based on the results shown in Fig. 1 and S1, it is expected that the amorphous structure is SnO_2, and the cubic-like structures are $CoSn(OH)_6$. Lin et al. reported that crystalline $CoSn(OH)_6$ had cubic-like structures.[34] Thus, our samples with cubic-like structures were considered as crystalline $CoSn(OH)_6$.

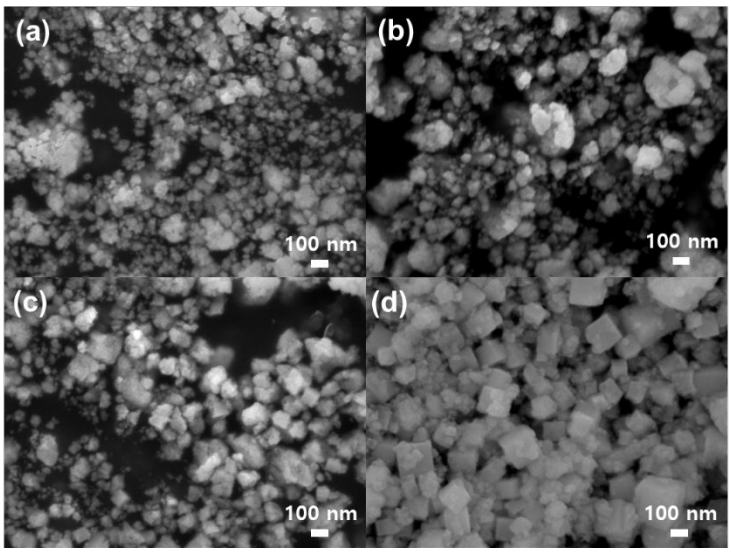

Figure 2. FE-SEM images of samples synthesized by SP at different pH; (a) CSO_ pH8sp, (b) CSO_pH9sp, (c) CSO_ pH 10sp, and (d) CSO_ pH 12sp.

TEM measurements were performed to observe the microstructures of the synthesized materials in detail. TEM images of the sample synthesized by SP under each condition are shown in Figure 3. Figure 3(a-b) confirmed that the samples for CSO_pH8sp, and CSO_pH9sp had amorphous and primary particle aggregated structures. On the other hand, in the samples of CSO_pH10sp and CSO_pH12sp, as shown in Fig. 3(c, e), amorphous and crystalline parts were mixed. The crystalline parts exhibited a cubic-like structure, which was similar in shape to that of $CoSn(OH)_6$, as reported by Song et al..[33] Thus, the cubic-like structure is considered to be $CoSn(OH)_6$. The sizes of a cubic-like structure are in the range of less than 100 nm. In high-resolution TEM (HRTEM) images (Fig. 3(d, f)), some vertical lattice patterns with the same interspacing of 0.38 nm corresponding to the (200) plane of $CoSn(OH)_6$ crystals are clearly visible.[49] In particular, the SAED patterns (Insets of Fig. 2(d, f)) of $CoSn(OH)_6$ show bright spots due to high crystalline properties.[50] From the results of XRD, TEM, and SAED patterns, it is concluded that the CSO_pH12sp sample had the most superior crystallinity among all samples synthesized in this study.

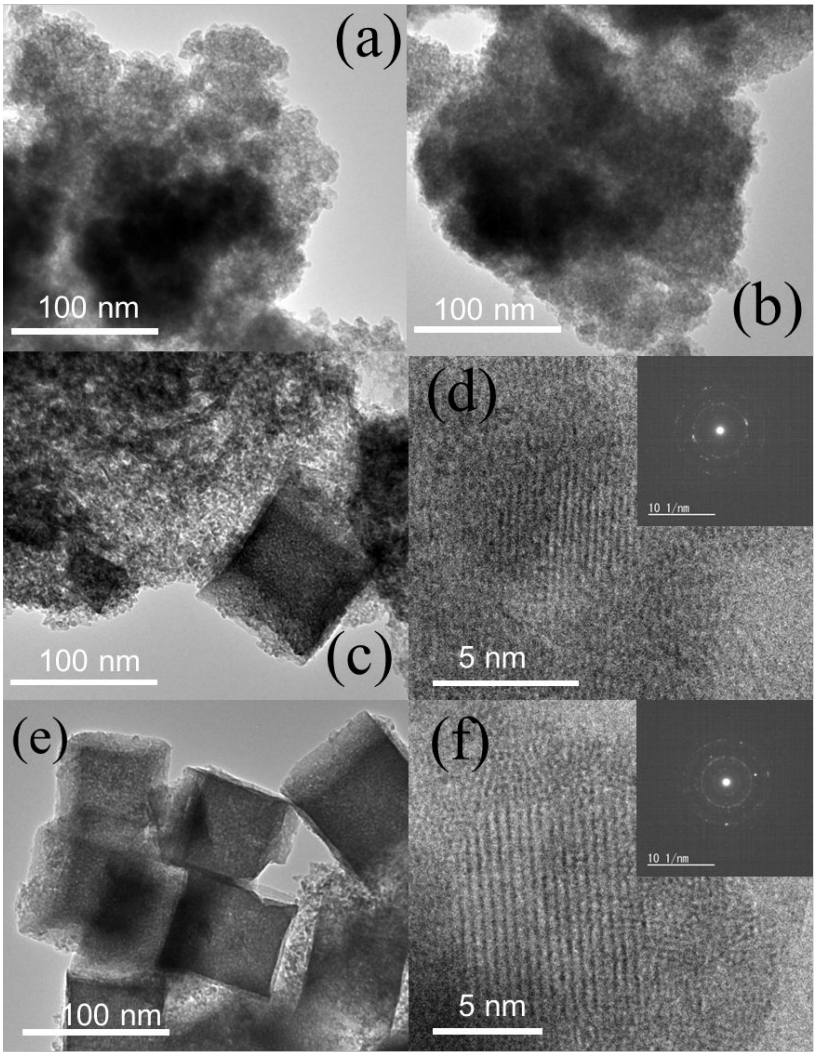

Figure 3. TEM images of the samples synthesized by SP at different pH: (a) TEM image of CSO_pH8sp, (b) TEM image of CSO_pH9sp, (c) TEM image of CSO_pH10sp, (d) HRTEM image of Fig. 3(c). The inset shows SAED pattern of cubic structure in Fig. 3(c), (e) TEM image of CSO_ph12sp, and (f) HRTEM image of Fig. 3(e). The inset shows SAED pattern of cubic structure in Fig. 3(e).

A TEM-EDS analysis was performed to investigate the structural composition. Figure 4 shows STEM images and elemental mapping images of Co, Sn, O, and W. Table 1 summarizes the atomic concentrations of each element obtained from the EDS results for each sample. As shown in Figure 4, the presence of Co, Sn, O, and W was confirmed in all the samples. W can be derived from the SP electrode material, and its content is very small, as shown in Table 1. It is presumed that this was sputtered by plasma and contained in the products.[50] The contrast of Co became darker as the pH of the solution increased, and the results in Table 1 also show that the Co content increased with an increase in the pH of the solution. This is because $Co(OH)_2$ is generated by increasing the pH, and $Co(OH)_2$ is reduced and oxidized by the active species in the plasma to form another Co compound. The STEM and elemental mapping images of CSO_pH10sp, and CSO_pH12sp revealed that Sn, Co, and O were well dispersed in the cubic-type framework. In addition, the Co/Sn ratios of CSO_10 and CSO_pH12sp were almost close to 1. By considering these in concert with the XRD results, it can be summarized that crystalline $CoSn(OH)_6$ was formed by SP.

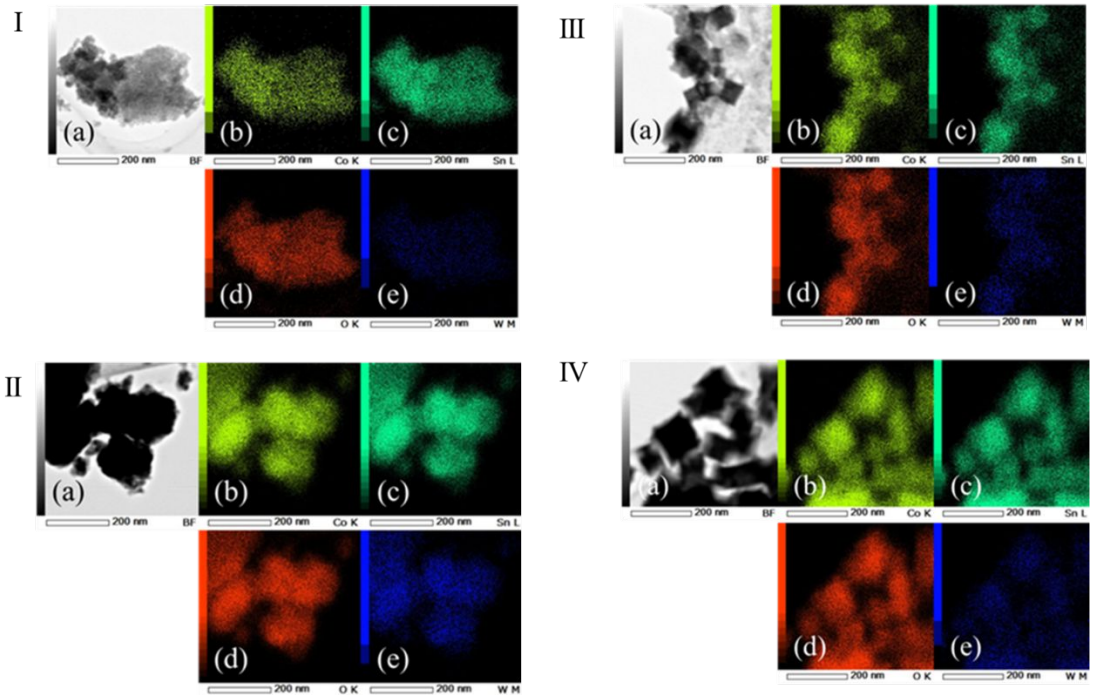

Figure 4. (a) STEM and (b) Co, (c) Sn, (d) O, and (e) W elemental mapping images of the samples synthesized by SP at different pH: (I) CSO_pH8sp, (II) CSO_pH9sp, (III) CSO_pH10sp, and (IV) CSO_pH12sp.

Table 1: Atomic Co, Sn, O, and W concentrations of the samples synthesized by SP at different pH: (a) CSO_pH8sp, (b) CSO_pH9sp, (c) CSO_pH10sp, and (d) CSO_pH12sp. (at%)

	Co	Sn	O	W
CSO_pH8sp	8.34	26.63	64.91	0.12
CSO_pH9sp	17.09	22.63	60.18	0.09
CSO_pH10sp	29.60	27.51	42.81	0.07
CSO_pH12sp	35.59	26.90	37.49	0.02

The compositions and binding states of the synthesized samples were investigated using XPS. The XPS Co 2*p* spectra of the samples are shown in Fig. 5. All Co_{2p} spectra are deconvoluted into two distinct peaks and two weak satellites. The two spin-orbit doublets assigned to cobalt oxides located at 780.7 and 796.7 eV correspond to $Co_{2p(3/2)}$ and $Co_{2p(1/2)}$, respectively.[50] The spin-orbit doublet of $Co_{2p(3/2)}$ can be deconvolved into two peaks at 780.5 and 782.1 eV assinged to the $Co^{3+}{}_{2p(3/2)}$ and $Co^{2+}{}_{2p(3/2)}$ configurations, respectively.[51] The $Co_{2p(1/2)}$ spin-orbital doublet can also be deconvoluted into two separate peaks located at binding energies of 796.4 and 797.5 eV, assigned to $Co^{3+}{}_{2p(1/2)}$ and $Co^{2+}{}_{2p(1/2)}$, respectively.[51] The presence of two satellite peaks ($Co_{sat.}$) near two spin-orbital doublets at binding energies of 787.0 and 802.6 eV further demonstrates the presence of cobalt oxides.[50,51] Figure 6 shows the high-resolution XPS Sn 3*d* spectra of the samples. In all samples, there are two peaks at 486.1–486.5 and 494.5–494.9 eV, which can be attributed to Sn $3d_{5/2}$ and $3d_{3/2}$, respectively. The energy separation of the observed spin is almost 8.4 eV, which means that Sn^{4+} is present in the synthesized sample.[49,51] The XRD patterns of the CSO_8, and CSO_9 samples exhibited some peaks derived from SnO_2, which is consistent with the XPS results. In addition, $CoSn(OH)_6$ was formed in the CSO_pH10sp, and CSO_pH12sp samples and the valence state of Sn in this compound was tetravalent. Therefore, the XPS results indicated that the compound synthesized in this study was $CoSn(OH)_6$.

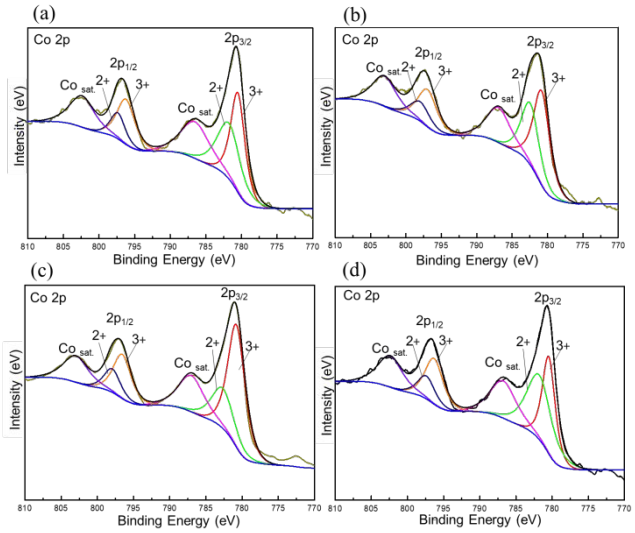

Figure 5. High-resolution XPS Co 2*p* spectra of the samples synthesized by SP at different pH:

(a) CSO_pH8sp, (b) CSO_pH9sp, (c) CSO_pH10sp, and (d) CSO_pH12sp.

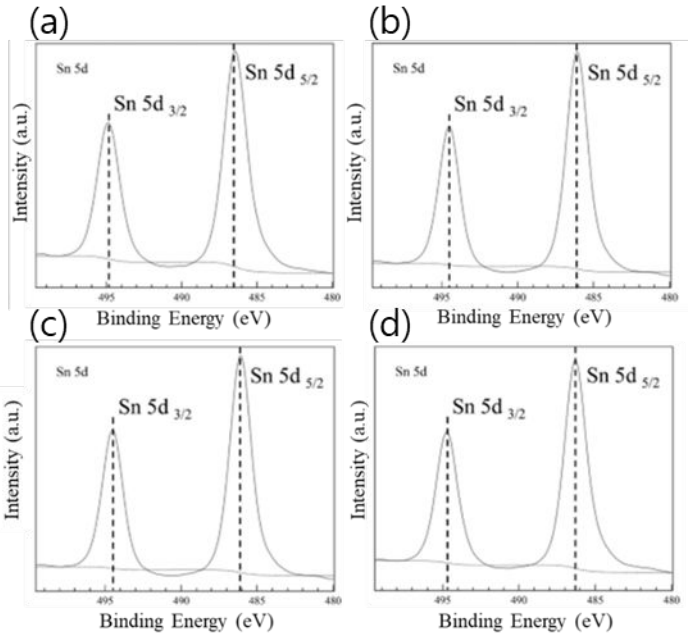

Figure 6. High-resolution XPS Sn 3*d* spectra of the samples synthesized by SP at different pH: (a) CSO_pH8sp, (b) CSO_pH9sp, (c) CSO_pH10sp, and (d) CSO_pH12sp.

.

Figure 7 shows the high-resolution XPS O1*s* spectra of the samples. The O1*s* spectrum is mainly composed of metal-oxygen bonds (Metal–O:530.6 eV) and metal–hydroxyl bonds (Metal–OH:531.7 eV), and the presence of oxygen and water adsorbed on the surface is also confirmed.[52,53]

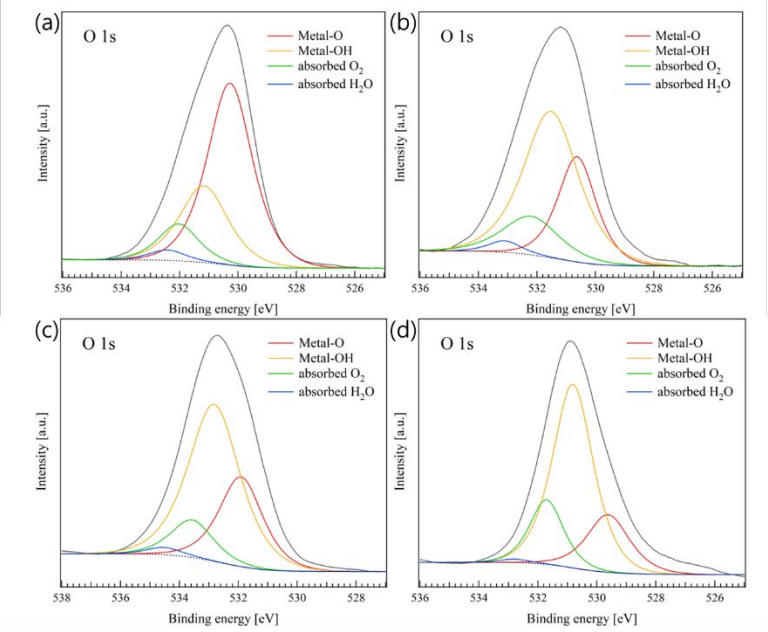

Figure 7. High-resolution XPS O1*s* spectra of the samples synthesized by SP at different pH: ~~(1)~~ (a) CSO_pH8sp, (b) CSO_pH9sp, (c) CSO_pH10sp, and (d) CSO_pH12sp.

Table 2 summarizes the composition near the surface of the compound obtained from the XPS spectra. From Table 2, it was confirmed that the main components of all the samples were Co, Sn, and O and that W derived from the electrodes was also present in the samples. According to the EDS results, the proportion of W was very small, but the proportion of W obtained from XPS was large. Based on this result, it can be found that many W-derived substances are present near the surface. Furthermore, the Co content in the sample increased with increasing pH. In addition, the ratio of Co to Sn approached 1:1 as the pH increased. From these results, it can be concluded that CSO_pH10sp and CSO_pH12sp formed $CoSn(OH)_6$.

Table 2. Atomic Co, Sn, O, and W concentrations of the sample surfaces synthesized by SP at different pH: (a) CSO_pH8sp, (b) CSO_pH9sp, (c) CSO_pH10, and (d) CSO_pH12sp. (at.%)

	O	Co	Sn	W
CSO_pH8sp	2.76	28.14	59.77	9.32
CSO_pH9sp	5.54	26.13	59.85	8.48
CSO_pH10sp	18.25	16.95	59.29	5.51
CSO_pH12sp	18.53	14.53	62.07	4.87

Figures 8 (a) and (b) showed the results of the optical emission spectroscopic analysis when CSO_pH12sp was synthesized by SP. Peaks and bands derived from H, O, OH, W, Co, and Sn were confirmed during the synthesis of CSO_pH12sp by SP. It is considered that H and OH radicals are derived from the decomposition of water, and O is derived from the decomposition of dissolved oxygen in water and solution.[54] W is derived from the electrode, and it is presumed that the W atom was sputtered from the electrode and mixed with the sample as an impurity. Co and Sn were derived from the raw materials Co^{2+} and Sn^{4+}.

The formation process of compounds containing Co and Sn was considered from the results of the confirmation of active species in the plasma. The H radical generated by SP is a powerful reducing species.[55] It is presumed that Co^{2+} and Sn^{4+} in the precursor solution can be reduced by H radicals and electrons generated in the plasma phase between the electrodes to form atomic Co and Sn, as shown in Equations (1) and (2).[56] In addition, because the pH of the mixed aqueous solutions of $CoCl_2$ and $SnCl_4 \cdot 5H_2O$ was 12, $Co(OH)_2$ and $Sn(OH)_4$ precipitates gradually formed with time evolution. These precipitates are affected by the local high-temperature state due to the generation of plasma, and the dehydration reaction can proceed. CoO and SnO_2 are also formed through the dehydration reaction, as shown in Equations (3) and (4), respectively. In addition, it

is speculated that compounds such as Co_3O_4 and SnO_2 are synthesized by the reaction of atomic Co and Sn with atomic O, which acts as an oxidizing species (Equations (5), (6), and (7)). Furthermore, it is considered that CoOOH was formed, as shown in Equation (8)[57], by the reaction between the formed CoO and OH radicals. However, because the peak intensities derived from Co_3O_4 and CoOOH in XRD are low, it is inferred that these formation reactions are randomly difficult. In the SP synthesis, the temperature of the entire solution was approximately room temperature. However, the electron temperature of the plasma phase generated between the electrodes is several thousand Kelvin, which is extremely high.[27] Thus, it is inferred that Co^{2+}, Sn^{4+}, and OH^- react, as shown in Equation (9),[58] to form $CoSn(OH)_6$ because of the influence of this local high-temperature region. In the synthesis of $CoSn(OH)_6$ using the co-precipitation method, the pH of the precursor solution was adjusted to 10 or more.[59] In this study, the presence of $CoSn(OH)_6$ was confirmed when synthesized at pH 10 or higher, suggesting that the synthetic route is the same as that of the co-precipitation method. The synthesis of $CoSn(OH)_6$ by the co-precipitation method requires several hours; however, in the case of SP, the chemical reaction can proceed in a plasma reaction field with locally high energy, and thus it is rapid. Thus, the

synthesis in a time of 20 min is considered to be possible. It is also possible that $Co(OH)_2$ and $Sn(OH)_4$ react directly to form $CoSn(OH)_6$, as shown in Equation (10).[60]

$$Co^{2+} + 2H\cdot \rightarrow Co + 2H^+ \text{ or } Co^{2+} + 2e^- \rightarrow Co \quad (1)$$

$$Sn^{4+} + 4H\cdot \rightarrow Sn + 4H^+ \text{ or } Sn^{4+} + 4e^- \rightarrow Sn \quad (2)$$

$$Co(OH)_2 \rightarrow CoO + H_2O \quad (3)$$

$$Sn(OH)_4 \rightarrow SnO_2 + 2H_2O \quad (4)$$

$$Co + O \rightarrow CoO \quad (5)$$

$$3Co + 4O \rightarrow Co_3O_4 \quad (6)$$

$$Sn + 2O \rightarrow SnO_2 \quad (7)$$

$$CoO + OH\cdot \rightarrow CoOOH \quad (8)$$

$$Co^{2+} + Sn^{4+} + 6OH^- \rightarrow CoSn(OH)_6 \quad (9)$$

$$Co(OH)_2 + Sn(OH)_4 \rightarrow CoSn(OH)_6 \quad (10)$$

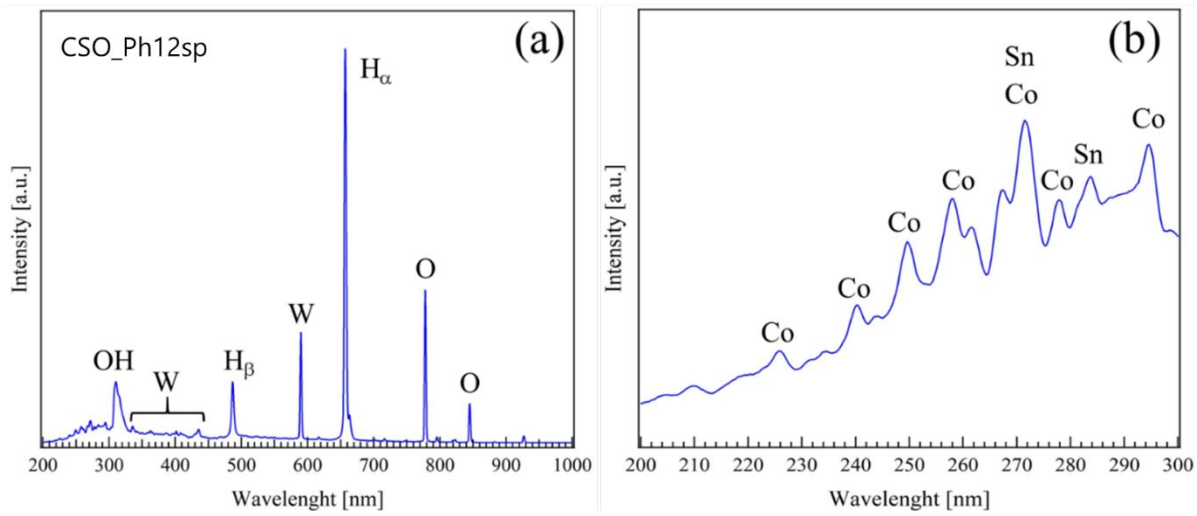

Figure 8. (a) OES spectrum of the sample synthesized by SP at pH =12, (b) Enlarged view of the spectrum (a) over the wavelength range of 200 to 300 nm.

The electrocatalytic properties of each synthesized sample and commercial RuO_2 powder for OER were evaluated using LSV. Figure 9 (a) shows the measurement results of the LSV at 1500 rpm for each sample, and Figure 9 (b) shows the Tafel plots immediately after the start of the OER. Table 3 summarizes the OER onset potentials, the potential values when the current density reached 10 mA/cm^2, and the Tafel gradient values for all samples synthesized by SP. With an increase in the solution pH for the synthesis of the samples, the current density increased as the potential was shifted to the noble direction. This indicates that the electrocatalytic

properties of the synthesized sample for the OER improved as the pH increased. As shown in Table 3, the OER onset potential of CSO_pH12sp was 1.470V vs. RHE, which was the noblest among the samples synthesized by SP. However, the OER onset potential of RuO_2, which has been conventionally used as a catalyst for the OER, was 1.475 V vs. RHE, and the value was as high as approximately 5 mV. From this result, it was found that the onset potential of the OER was slightly inferior to that of RuO_2. In contrast, regarding the potential when the current density reached 10 mA/cm^2, that of CSO_pH12sp was the lowest, which was lower than that of RuO_2 by 104 mV vs. RHE. The overpotentials, η, of CSO_pH12sp, CSO_pH10sp, and RuO_2 at 10 mA/cm^2 were estimated to be 350, 395, and 454 mV, respectively, and CSO_pH10sp and CSO_pH12sp showed a lower overpotential than commercial RuO_2. This result indicates that CSO_pH12sp synthesized by SP has excellent electrocatalytic properties compared to those of RuO_2. Song et al. reported the $CoSn(OH)_6$ nanocube synthesized by a co-precipitation and electrochemical preconditioning showed an overpotential of 363 mV at 10 mA/cm^2.[33] The η of CSO_pH12sp at 10 mA/cm^2 was 13 mV lower than that of the $CoSn(OH)_6$ nanocube synthesized by a co-precipitation and electrochemical preconditioning without any pretreatment. This indicates that the CSO_pH12sp sample has more superior electrocatalytic properties than the

$CoSn(OH)_6$ nanocubes with porous structures synthesized by co-precipitation and electrochemical preconditioning. As shown in Figure S3 and Table S1, all samples synthesized by co-precipitation method in this study also showed OER activity. The OER onset potential of CSO_pH8p, CSO_pH 9p, CSO_pH10p, and CSO_pH 12p tended to increase with an decrease in the solution pH and the overpotentials at 10 mA/cm^2 decreased with an increase in the solution pH. However, in case of CSO synthesized from same solution pH, the electrocatalytic properties of CSO synthesized by co-precipitation were inferior to those synthesized by SP. Regarding the Tafel gradient value, which is an index of OER activity, CSO_pH12sp showed the lowest value of 69.58 mV/decade. The Tafel gradient value of CSO_pH10sp was 72.54 mV/decade. In contrast, the Tafel gradient value of commercially available RuO_2 was 71.23 mV/decade, which was a slightly higher value than CSO_pH12sp. From these results, it can be concluded that the CSO_pH12sp synthesized in this study showed excellent electrocatalytic properties for OER, which was superior to commercial RuO_2. Double-layer capacitance (C_{dl}) measurements were performed to determine the electrochemically active surface area (ECSA) of CSO_pH10sp and CSO_pH12sp using cyclic voltammetry in 1 M KOH. The ECSA can be calculated using the C_{dl} values and the following equation[61]:

$$ECSA = C_{dl} / C_s$$

where C_s shows a specific capacitance. In case of using 1 M KOH aqueous solution, the C_s value is 0.040 mF/cm^2 depending on the typical reported values.[61] The ECSA indicates how activated the OER response is, the higher the value, the better the performance. The C_{dl} values for CSO_pH10sp and CSO_pH12sp were estimated to be 0.73 and 1.42 mF/cm^2, respectively. Using these values, the ECSA values for CSO_pH10sp and CSO_pH12sp were found to be 18.39 and 35.40, respectively. This indicates that the OER response of the CSO_pH12sp is higher than that of CSO_pH10sp. Thus, the electrocatalytic activity of CSO_pH12sp for OER were considered to show the most superior performance among all samples. The long-term durability of the OER are important characteristics of catalysts for realizing practical applications of metal-air battery. The most active CSO_pH12sp was used for the durability test in this study. The current-time chronoamperometric response was performed at a constant overpotential of 0.35 V vs. RHE in an O_2-saturated 1 M KOH solution to assess the durability of the most active CSO_pH12sp, as shown in Fig. 9(f). The current density was slightly decreased in a few hundreds seconds and remained constant at approximately 10 mA/cm^2. The current density values were kept almost constant value of 10 mA/cm^2 after 45,000 s of continuous operation. To investigate change in the surface states and crystallinity of the CSO_pH12sp after the CA test for 45000 s, XPS and XRD measurements were performed. The high-resolution XPS Co 2*p*, Sn 5*d* and O 1*s* specta are shown in Figure S4. These XPS spectra showed no significant peak change after the CA tests (Figure S4). The relative ratio of Co^{3+} content slightly increased after CA test. This could be caused by electrochemical oxidation. Co^{3+} is known to play an important role in OER activities

and is reported to contribute the improvement of durability.[65] In addition, the XRD pattern of the CSO_pH12sp before and after the CA test for 45000 s are also shown in Figure S5. From the XRD patterns of Fig. S5, no change in crystal phase could be observed. These results confirm that CSO_pH12sp has superior long-term durability in 1 M KOH solution.

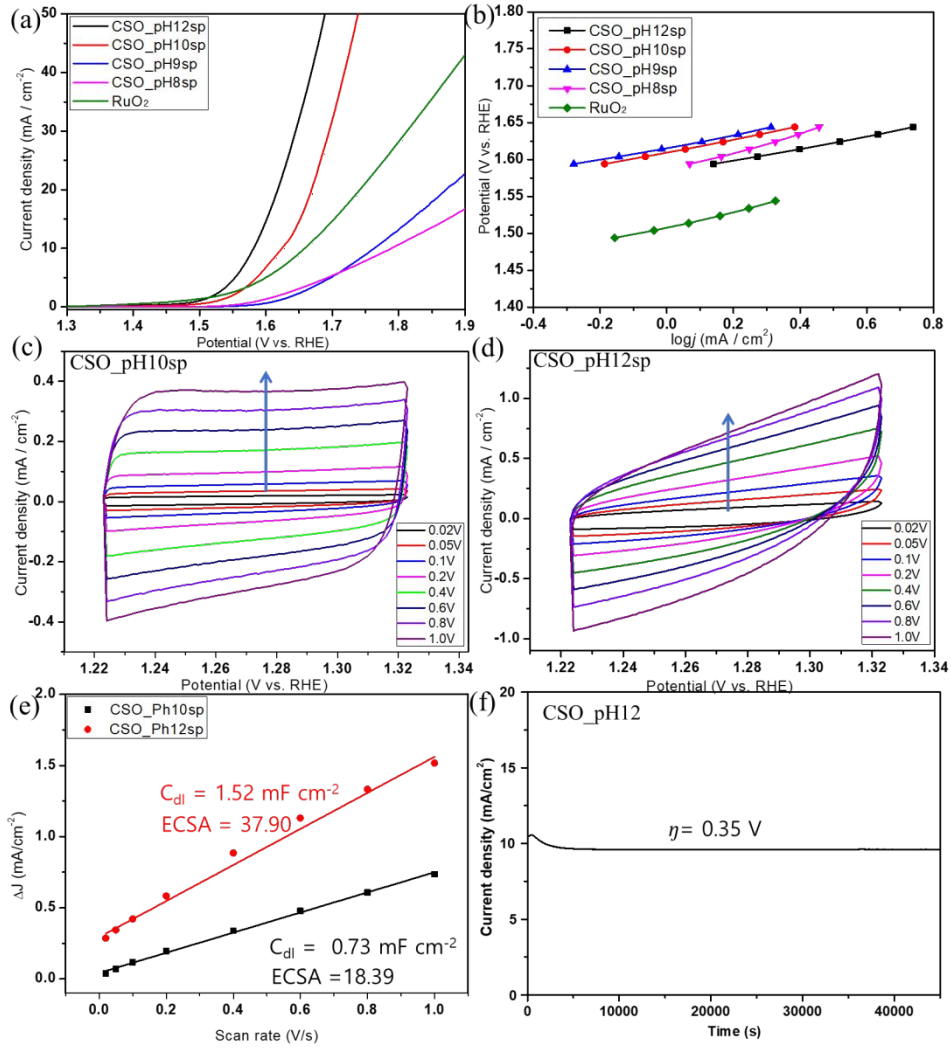

Figure 9. (a) Linear sweep voltammogram of the samples synthesized at different pH and commercial RuO_2, and (b) Tafel slopes of the samples synthesized at different pH and commercial

RuO_2. CVs of (c) CSO_pH10sp and (d) CSO_pH12sp measured in 1.0 M KOH at scan rates of 0.02 to 0.1 V s^{-1} (e) Electrochemical double layer capacitance (C_{dl}) at 1.273 V vs. RHE of CSO_pH10sp and CSO_pH12sp. (f) Chronoamperometric (CA) curve of CSO_pH12sp at an overpotential of 0.35 V vs. RHE after 45000 s.

Table 3 OER onset potentials, potentials at reaching 10 mA/cm^2, overpotentials at 10 mA/cm^2, and Tafel slope of the samples synthesized at different pH, commercial RuO_2, and reported values.

Sample	OER Onset Potentials [V vs. RHE]	Potentials at reaching 10 mA/cm^2 [V vs. RHE]	Overpotentials at 10 mA/cm^2 [V vs. RHE]	Tafel Slope [mV/dec.]
CSO_pH12sp	1.480	1.580	0.350	69.58
CSO_pH10sp	1.540	1.625	0.395	72.54
CSO_pH9sp	1.558	1.763	0.533	78.44
CSO_pH8sp	1.545	1.790	0.560	82.76
RuO_2	1.475	1.659	0.429	73.34
CoSn-T1[33]	-	1.593	0.363	-
CoSn-T2[33]	-	1.627	0.397	-
CoSn-T3[33]	-	1.665	0.435	-
Co_3O_4[62]		1.760	0.530	-
$Co_3O_{4-\delta}$[63]		1.620	0.400	-

CoSn indicates crystalline $CoSn(OH)_6$. T1, T2 and T3 mean ultrasonic bath temperature (T1: 0℃, T2: 23℃, T3: 54℃) during crystal growth. CoSn-T1, T2, and T3 are samples after electrochemical preconditioning.

Figure 10 shows a schematic diagram of the OER catalyst mechanism for Co species.[64] As shown in Figure 10, it is considered that the Co species deprive the OH^- of electrons to generate O· as an intermediate, and O· becomes the active site for the OER. It is presumed that the number of OER active sites increases and the catalytic performance improves as the proportion of the compound containing Co increases with increasing pH. In addition, hydroxides composed of multiple metals, such as $CoSn(OH)_6$ have higher electrical conductivity than hydroxides composed of one metal.[49] As a result, CSO_pH10sp and CSO_pH12sp, containing $CoSn(OH)_6$ are more likely to transfer electrons than CSO_pH9sp, containing SnO_2 and CoOOH, and it is thus considered that the catalytic performance toward the OER is improved.

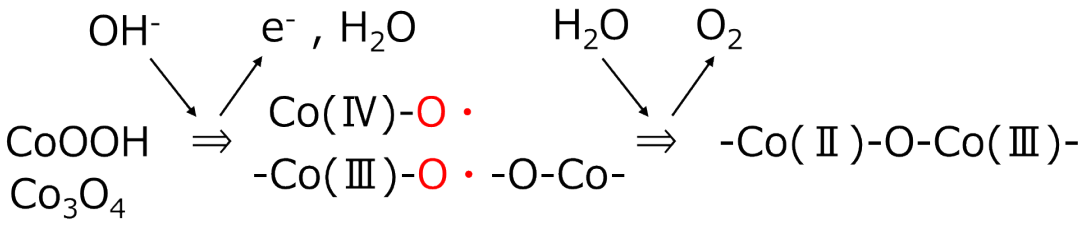

Figure 10. Schematic diagram of the catalytic mechanism for compounds containing Co species.

4. Conclusions

CSO materials were successfully synthesized by SP and co-precipitation method from aqueous solutions at pH of 10 to 12, and were characterized by XRD, FE-SEM, and TEM. When the precursor solution had a pH of 9 or less, SnO_2 was generally synthesized. However, when the precursor solution had a pH of 10 or higher, CSO was generally formed. Notably, more CSO was obtained when the pH of the precursor solution was higher. It was observed that the crystallinity of the CSO synthesized by SP was increased and the size of the nanocube structure was approximately 100 nm. On the other hand, the size of the nanocube structure synthesized by co-precipitation was approximately 200 nm. We found that the synthesis time of CSO using SP was shorter than that by co-precipitation method. From the OES results, the chemical species formed in the plasma (SP) were identified, and the mechanism of product synthesis was discussed.

The electrocatalytic properties of CSO for OER improved with the increasing pH of the precursor solution used for the synthesis of SP and co-precipitation. The improvement in electrocatalytic performance is attributed to the increase in the OER active sites due to the increase in the proportion of the compound containing Co. In case of CSO synthesized using same solution pH, the electrocatalytic properties of CSO synthesized by SP were superior to those synthesized by co-precipitation method. Among the synthesized samples, the OER onset

potential of CSO_pH12sp was 1.470V vs. RHE, which was the lowest value. When the potential reached 10 mA/cm^2, CSO_pH12 had the lowest potential, which was 104 mV lower than that of commercial RuO_2. The overpotential at 10mA/cm^2 and Tafel gradient of the CSO_pH12sp were estimated to be 350 mV and 69.58 mV/decade, respectively. The CSO_pH12sp sample showed most superior catalytic property among all samples synthesized and the catalytic property was superior to commercial RuO_2. The OER is an extremely important chemical reaction for improving storage batteries and water splitting. Perovskite-type oxides are promising catalyst materials for improving OER efficiency. SP is an effective process for the synthesis of nanomaterials. In the future, we hope that other perovskite-type oxide nanomaterials will be synthesized by SP process and developed into storage batteries for water splitting.

Conflicts of interest

There are no conflicts to declare.

Acknowledgments

This work was supported by the Strategic International Collaborative Research Program (SICORP) grant number JPMJSC18H1, from the Japan Science and Technology Agency (JST), and a Grant-in-Aid for Challenging Research Exploratory (No. 21K18835) from the Japan Society for the Promotion of Science (JSPS).

References

1. G. Girishkumar, B. McCloskey, A. Luntz, S. Swanson, and W. Wilcke, *J. Phys. Chem. Lett.*, **2010**, 1, 2193–2203.
2. K.-N. Jung, J.-h. Kim, Y. Yamauchi, M.-S. Park, J.-W. Lee, and J. H. Kim, *J. Mater. Chem.*, **2016**, 4, 14050–14068.
3. J. Kang, O. L. Li, and N. Saito, *J. Power Sources* **2014**, 261, 156-161.
4. W. Meng, L. Wen, Z. Song, N. Cao, and X. Qin, *J. Solid State Electrochem.*, **2017**, 21(3), 665-671.
5. Y. Zhang, H. Zhang, J. Lia, M. Wang, H. Nie, and F.X. Zhang, *J. Power Sources*, **2013**, 240, 390-396.
6. N. Ding, S. W. Chien, T. S. Andy. Hor, R. Lum, Y. Zonga, and Z. Liu, *J. Mater. Chem. A*, **2014**, 2, 12433-12441.
7. Y. Chen, F. Li, D.-M. Tang, Z. Jian, C. Liu, D. Golberg, A. Yamada, and H. Zhou, *J. Mater. Chem. A*, **2013**, 1, 13076-13081.
8. J. Xiao, D. Mei, X. Li, W. Xu, D. Wang, G.L. Graff, W.D. Bennett, Z. Nie, L.V. Saraf, I.A. Aksay, J. Liu, and J.-G. Zhang, *Nano Lett.*, **2011**, 11, 5071-5078.
9. L. Tian, J. Wang, K. Wang, H. Wo, X. Wang, W. Zhuang, T.X. Li, and X. Du, *Carbon*, **2019**, 143, 457-466.
10. Y. Zhao, J. Zhang, W. Wu, X. Guo, P. Xiong, H. Liu, and G. Wang, *Nano Energy*, **2018**, 54, 129-137
11. Q. Dong, Z.Y. Mo, H. Wang, S. Ji, X.Y. Wang, V. Linkov, and R.F. Wang, *ACS Sustain. Chem. Eng.*, **2020**, 8, 6979-6989.

12. H.S. Kim, M. Kim, M.S. Kang, J. Ahn, Y.-E. Sung, and W.C. Yoo, *ACS Sustain. Chem. Eng*., **2018**, 6, 2324-2333.
13. C. Maouche, Y.Z. Zhou, B. Li, C. Cheng, Y.Y. Wu, J.H. Li, S. Gao, and J. Yang, *J. Electroanal. Chem*., **2019**, 853, 113536.
14. H.-J. Lu, Y. Li, L.-Q. Zhang, H.-N. Li, Z.-X. Zhou, A.-R. Liu, Y.-J. Zhang, and S.-Q. Liu, *RSC Adv*., **2015**, 5, 52126-52131.
15. Y.Z. Zhou, C.H. Yen, S.F. Fu, G.H. Yang, C.Z. Zhu, D. Du, P.C. Wo, X.N. Cheng, J. Yang, C.M. Wai, and Y.H. Lin, *Green Chem*., **2015**, 17, 3552-3560.
16. Z.-L. Jiang, H. Sun, W.-K. Shi, J.-Y. Cheng, J.-Y. Hu, H.-L. Guo, M.-Y. Gao, H.J. Zhou, and S.-G. Sun, *ACS Sustain. Chem. Eng*., **2019**, 7, 14161-14169.
17. C.C. Xu, Y. Su, D.J. Liu, and X.Q.He, *Phys. Chem. Chem. Phys*., **2015**, 17, 25440-25448.
18. C.C. Yao, J.X. Li, Z.H. Zhang, C.L. Gou, Z.S. Zhang, G. Pan, and J. Zhang, *Small*, **2022**, 2108094.
19. N. Chawla, A. Chamaani, M. Safa, and B. El-Zahab, *J. Electrochem. Soc.*, **2017**, 164, A6303-6307.
20. S. Ma, Y. Wu, J. Wang, Y. Zhang, Y. Zhang, X. Yan, Y. Wei, P. Liu, J. Wang, K. Jiang, S. Fan, Y. Xu, and Z. Peng, *Nano Lett*., **2015**, 15, 8084-8090.
21. Y. Chen, S. Ji, Y. Wang, J. Dong, W. Chen, Z. Li, R. Shen, L. Zheng, Z. Zhuang, D. Wang, and Y. Li, *Angew. Chem. Int. Ed*., **2017**, 56, 6937-6941.
22. Y. Yui, S. Sakamoto, M. Nohara, M. Hayashi, J. Nakamura, and T. Komatsu, *J. Power Sources*, **2017**, 340, 121-125.
23. R. Liang, A. Hu, M. Li, Z. Ran, C. Shu, and J. Long, *J. Alloys Compds*., **2019**, 810, 151877.
24. Y.J. Lee, D.H. Kim, T.-G. Kang, Y. Ko, K. Kang, and Y.J. Lee, *Chem. Mater*., **2017**, 29, 10542-10550.
25. I. Yamada, and S. Yagi, The *Review High-Pressure Sci. Technol*., **2016**, 26, 247-252.
26. S. Yagi, H. Ikeno, and I. Tamada, *J. MMIJ*, **2017**, 133, 264-269.
27. K.A. Stoerzinger, W. Lü, C. Li, Ariando. T. Venkatesan, and S.-H. Yang, *J. Phys. Chem. Lett*., **2015**, 6, 1435-1440.
28. A. Grimaud, C.E. Carlton, M. Risch, W.T. Hong, K.J. May, and Y. Shao-Horn, *J. Phys. Chem. C*, **2013**, 117, 25926-25932.
29. X. Cheng, E. Fabbri, M. Nachtegaal, I.E. Castelli, M.E. Kazzi, R. Haumont, N. Marzari, and T.J. Schmidt, Oxygen Evolution Reaction on $La_{1-x}Sr_xCoO_3$ Perovskites: A Combined Experimental and Theoretical Study of Their Structural, Electronic, and Electrochemical Properties, *Chem. Mater*., **2015**, 27, 7662-7672.
30. J. Suntivich, K.J. May, H.A. Gasteiger, J.B, *Science*, **2011**, 334, 1383-1385.
31. A. Grimaud, K.J. May, C.E. Carlton, Y.L. Lee, M. Risch, W.T. Hong, J. Zhou, and Y. Shao-Horn, *Nat. Commun*., **2013**, 4, 2439.

32. J. Kim, X. Yin, K.C. Tsao, S. Fang, and H. Yang, *J. Am. Chem. Soc*., **2014**, 136, 14646-14649.
33. F. Song, K. Schenk, and X. Hu, *Energy Environ. Sci*., **2016**, 9, 473-477.
34. X. Lin, Y. Gao, M. Jiang, Y. Zhang, Y. Hou, W. Dai, S. Wang, and Z. Ding, *Appl. Catalysis B: Environ*., **2018**, 224, 1009-1016.
35. P. Pootawang, N. Saito, and O. Takai, *Mater. Lett*., **2011**, 65, 1037-1040.
36. A. Watthanaphanit, and N. Saito, Effect of polymer concentration on the depolymerization of sodium alginate by the solution plasma process, *Polym. Degrad. Stabil*., 2013, 98, 1072-1080.
37. J. Kang, O. L. Li, and N. Saito, *Carbon*, **2013**, 60, 292-298.
38. T. Ishizaki, S. Chiba, Y. Kaneko, and G. Panomsuwan, *J. Mater. Chem. A*, **2014**, 2, 10589-10598.
39. G. Panomsuwan, N. Saito, and T. Ishizaki, *Phys. Chem. Chem. Phys*. **2015**, 17, 6227-6232.
40. G. Panomsuwan, N. Saito, and T. Ishizaki, *J. Mater. Chem. A*., **2015**, 3, 9972-9981.
41. G. Panomsuwan, N. Saito, and T. Ishizaki, *ACS Appl. Mater. Interfaces*, **2016**, 8, 6962-6971.
42. O.L. Li, S. Chiba, Y. Wada, H.S. Lee, and T. Ishizaki, *RSC Adv*., **2016**, 6, 109354-109360.
43. T. Ishizaki, Y. Wada, S. Chiba, S. Kumagai, H.S. Lee, A. Serizawa, O.L. Li, and G. Panomsuwan, *Phys. Chem. Chem. Phys*., **2016**, 18, 21843-21851.
44. G. Panomsuwan, N. Saito, and T. Ishizaki, *Carbon*, **2016**, 98, 411-420.
45. C. Chokradjaroen, S. Kato, K. Fujiwara, H. Watanabe, T. Ishii, and T. Ishizaki, *Sustain. Energy Fuels*, **2020**, 4, 4570 - 4580.
46. O.L. Li, S. Chiba, Y. Wada, G. Panomsuwan, and T. Ishizaki, *J. Mater. Chem. A*, **2017**, 5, 2073 - 2082.
47. G. Panomsuwan, N. Saito, T. Ishizaki, *ACS Appl. Mater. Interfaces*, **2016**, 8, 6962–6971 (2016).
48. G. Panomsuwan, J. Chantaramethakul, C. Chokradjaroen, T. Ishizaki, *Mat. Lett*., 2019, 251, 135–139.
49. B. K. Satpathy, C. R. Raj and D. Pradhan, *Electrochim. Acta*, **2022**, 433, 141250
50. G. Aruchamy and S. Thangavelu, *Electrochim. Acta*, **2020**, 344, 136141.
51. C. Shang, S. Dong, P. Hu, J. Guan, D. Xiao, X. Chen, L. Zhang, L. Gu, G. Cui and L. Chen, *Sci. Rep.*, 2015, **5**, 8335.
52. J. Zhou, Y. Zhao, L. Qin, C. Zeng, and E. Xiao, *Funct. Mater. Lett.*, **2016**, 9, 1642009.
53. R. Sahoo, A.K. Sasmal, C. Ray, S. Dutta, A. Pal, and T. Pal, *ACS Appl. Mater. Interfaces*, **2016**, 8, 17987-17998.
54. M.A. Bratescu, S.P. Cho, O. Takai, and N. Saito, *J. Phys. Chem. C*, **2011**, 115, 24569-24576.
55. M.A. Bratescu, O. Takai, and N. Saito, *J. Alloys Compds*., **2013**, 562, 74-83.
56. Q. Chen, T. Kaneko, and R. Hatakeyama, *Appl. Phys. Express*, **2012**, 5, 086201.

57. V. Pralong, A. Delahaye-Vidal, B. Beaudoin, B. Gerand, and J. Tarascon, *J. Mater. Chem.*, **1999**, 9, 955-960.
58. Z. Yang, C. Li, F. Liu, X. Lv, L. Zhang, Y. somg, and H. Wang, *Molecules*, **2022**, 27, 7960.
59. S. Subbarayan, M. Natesan, and S.-M. Chen, *New J. Chem*., **2020**, 44, 11271-11281.
60. Z. Wang, Z. Wang, H. Wu, and X. W. Lou, *Sci. Rep.*, **2013**, 3, 1391.
61. C. C. McCrory, S. Jung, J. C. Peters, and T. F. Jaramillo, J. Am. Chem. Soc., 2013, 135, 16977-16987.
62. Y. Sun, S. Gao, F. Lei, J. Liu, L. Liang, and Y. Xie, *Chem. Sci.*, **2014**, 5, 3976-3982.
63. Y. C. Wang, T. Zhou, K. Jiang, P. M. Da, Z. Peng, J. Tang, B. A. Kong, W. B. Cai, Z. Q. Yang, and G. F. Zheng, *Adv. Energy Mater.*, **2014**, 4, 1400696.
64. A. Moysiadou, S. Lee, C.-S. Hsu, H.M. Chen, and X. Hu, *J. Am. Chem. Soc*., **2020**, 142, 11901-11914.
65. Z. W. Gao, T. Ma, X. M. Chen, H. Liu, L. Cui, S. Z. Qiao, J. Yang and X. W. Du, *Small*, **2018**, 14, 1800195.